Article

Conductive Polyaniline−Indium Oxide Composite Films Prepared by Sequential Infiltration Synthesis for Electrochemical Energy Storage

Jiwoong Ham, Sangbaek Park, and Nari Jeon*

Cite This: *ACS Omega* 2023, 8, 946−953

Read Online

ACCESS | Metrics & More | Article Recommendations | Supporting Information

ABSTRACT: Composites of conductive polymers (CP) and metal oxides (MO) have attracted continued interest in the past decade for diverse application fields because the synergistic effects of CP and MO enable the realization of unusual electronic, electrochemical, catalytic, and mechanical properties of the composites. Herein, we present a novel method for the sequential infiltration synthesis of composite films of polyaniline (PANI) and indium oxide (InO_x) with high electrical conductivities (4−9 S/cm). The synthesized composite films were composed of two phases of graded concentration: InO_x with oxygen vacancies and PANI with partially protonated molecular units. The PANI−InO_x composite films displayed enhanced electrochemical activity with a pair of well-defined redox peaks. The open interfacial regions between the InO_x and PANI phases may provide efficient pathways for ion diffusion and active sites for improved charge transfer.
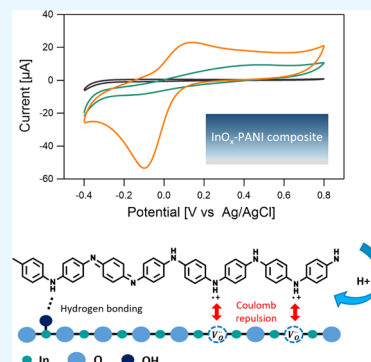
INTRODUCTION

Composites of conductive polymers (CP) and metal oxides (MO) are useful in a variety of fields, including sensors,[1] drug delivery,[2] catalysts,[3] and supercapacitors,[4] owing to their unique and versatile properties such as tunable electrical conductivity, stretchability, and electrochemical activity.[5−7] The various properties of the composite materials depend on the types of synthetic methods and specific experimental conditions that determine the chemical composition and its distribution, doping, and oxidation states of the composites. Therefore, the development of new techniques for the synthesis of CP-MO composites has gained considerable attention. Previously, wet chemical methods for the preparation of CP in different forms such as thin films, foams, gels, and fibers have been well established.[8−10] It is anticipated that combining vapor-based processes to incorporate inorganic components or modify doping in the CP of predefined forms can provide new opportunities to realize CP-MO composites with desired structures and properties.

Sequential infiltration synthesis (SIS) is one of the subcategories of atomic layer deposition (ALD), and it has recently emerged as a promising way to prepare organic− inorganic composite films with excellent control over their morphologies.[11−14] The following are the major SIS growth mechanisms: (1) precursor infiltration into the polymer matrix; (2) reversible/irreversible reaction of the precursor with specific functional groups of the polymer; and (3) chemical reactions between precursors and coreactant precursors within the polymer matrix.[15−17] Various compositional and structural factors of the composite films, such as the ratio of organic-to-inorganic components and the distribution

of the chemical composition, can be controlled by varying the SIS conditions, such as the growth temperature, precursor exposure time, and precursor purge time.[16] Therefore, SIS is expected to be useful for preparing CP-MO composites with the content and distribution of MO carefully controlled.

However, only a few studies have reported SIS using conductive polymers. Earlier studies included the doping of polyaniline (PANI) using metal precursors of Lewis acidic nature without the use of coreactants and the formation of PANI−oxide composites such as PANI−ZnO,[18] and PANI− TiO_x.[19] One of the main goals of the previous works was to increase the electrical conductivities of the doped PANI or PANI−oxide composite films to levels comparable to those of PANI doped with HCl via conventional solution processes.[20] While PANI−oxide composite films prepared via different methods have been reported to present improved mechanical, thermal, and electrochemical properties,[5−7] composite films prepared via SIS have rarely been explored.[21]

Herein, we present SIS as a facile synthetic route for preparing PANI−InO_x composite films. The films exhibited an enhanced electrical conductivity of 4−9 S/cm after annealing in a reducing atmosphere. Characterization via X-ray photoelectron spectroscopy revealed a graded concentration of InO_x in the PANI matrix, with greater oxygen vacancy concentration
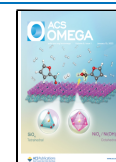
in the PANI-rich regions. The combination of UV−vis spectroscopy, Raman spectroscopy, and Fourier transform infrared (FTIR) spectroscopy showed that the molecular structures of PANI with quinonoid segments were partly converted to benzenoid segments along with the formation of protonated imine/amine. The PANI−InO$_x$ composite films presented a well-defined redox peak with improved charge storage capabilities compared with single-phase PANI and single-phase InO$_x$ films under neutral aqueous conditions. The enhanced electrochemical properties were attributed to the possible chemical interactions between PANI and InO$_x$ at their interfaces.

EXPERIMENTAL SECTION

Sample Preparation. SIS was performed using a cross-flow ALD reactor that contained a 4 wafer. PANI and N-Methyl-2-pyrrolidone (NMP) were purchased from Sigma-Aldrich (99%). The 3 wt % PANI−NMP solution was prepared by stirring it for 24 h at room temperature. PANI thin films were prepared on Si or FTO-coated glass substrates by spin coating at a spin speed of 2000 rpm. The Si and FTO/glass substrates had 500 nm thick SiO$_2$ layers and 600 nm thick FTO layers, respectively. The InO$_x$ SIS cycle consists of trimethylindium (TMIn) and H$_2$O half-cycles. The TMIn (H$_2$O) half-cycle was composed of a 1 s dose, 120 s exposure, and 120 s purge. During the exposure step, the gate valve between the main chamber and pump was closed, and a constant flow of Ar was provided. The SIS-prepared samples were annealed at 280 °C for 1 h in a tube furnace with a temperature ramp-up rate of 7 °C/min. The annealing was performed either in air or in the forming gas (3% H$_2$ in N$_2$).

Sample Characterization. The PANI−InO$_x$ thin films were gently scratched using a tweezer to create a step, and the step height was measured using a surface profiler (D-500, KLA tencor). An InO$_x$ thin film grown on a bare Si substrate without a polymer layer was wet-etched by partially dipping the samples in 1.35 M oxalic acid at 65 °C for ∼20 min. The sheet resistances of the samples were measured using a four-point probe measurement system (CMT-SR2000N, AIT), which was later converted into conductivity by considering the measured film thickness. Scanning electron microscope (SEM) imaging was performed on the samples, whose surfaces were coated with Pt for sputtering for 60 s, using Clara and Tescan with an electron-beam energy of 10 keV and an electron-beam current of 100 pA. X-ray photoelectron spectroscopy (XPS) was performed using an XPS photoelectron spectrometer (K-α^+, Thermo Scientific) with an X-ray source of microfocused monochromatic Al Kα (1487 eV) and a spot size of 100 μm. The BE of the HRXPS was calibrated using a C 1s spectra with an adventitious C peak at 284.8 eV. The Raman spectrometer, LabRAM HR-800 (Horiba Jobin Yvon), was used for Raman spectroscopy measurements under the following conditions: 514 nm excitation laser, 1800 grating, 0.1% neutral density filter, 5 s acquisition time, and 5 spectral accumulations. Attenuated total reflectance—Fourier transform infrared (ATR-FTIR) spectra were collected using an FTIR spectrometer (α-P, Bruker) equipped with a DTGS detector with a spectral resolution of 4 cm^{-1}. For the cyclic voltammetry (CV) experiments, an electrochemical analyzer (CHI602E, CH Instruments) was used with a three-electrode setup consisting of a Pt mesh counter electrode, Ag/AgCl reference electrode, and the working electrode of the sample being measured. Buffer solutions with different pH values were used as aqueous

electrolytes. For electrochemically active surface area (ECSA) measurements, CVs at various scan rates were recorded in a potential range of ±100 mV with respect to the open circuit potential using a 0.1 M NaCl aqueous solution as the electrolyte. Galvanostatic charge−discharge (GCD) curve and electrochemical impedance spectroscopy (EIS) tests were performed using a pH 7 phosphate buffer saline solution under the three-electrode system described above. For GCD, EIS, and two-electrode tests, an electrochemical analyzer (Vertex, IVIUM Technologies) was used. The selected potential and current ranges were from −0.4 to +0.8 V, and from +20 μA (for charging) to −20 μA (for discharging), respectively. The EIS experiments were performed under an applied voltage of 0.1 V with a frequency range of 0.01 Hz to 1 MHz.

Results and Discussion. Figure 1a shows the sample preparation process, which includes spin coating, SIS, and annealing. We mainly dealt with two types of substrates: a
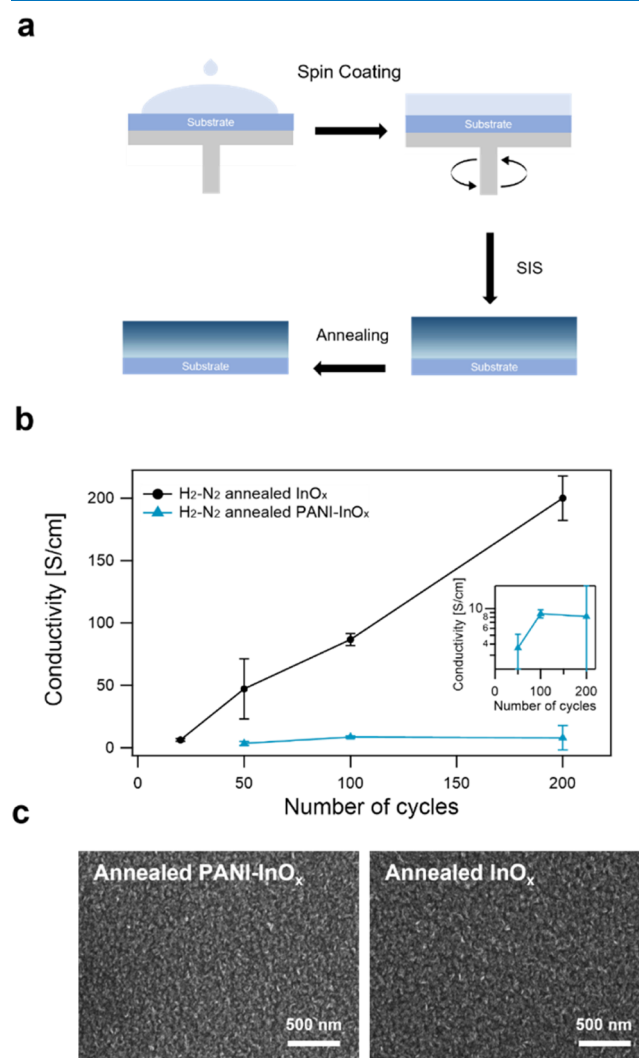

Figure 1. (a) Schematic of the sample preparation procedure, including spin coating of polyaniline, InO$_x$ SIS, and annealing. (b) Electrical conductivities of the H$_2$−N$_2$ annealed PANI−InO$_x$ and InO$_x$ samples as a function of SIS cycle number. The error bars were obtained from the measurement of four samples in each condition. (c) SEM images of the annealed PANI−InO$_x$ and InO$_x$ samples grown with 50 SIS cycles.

PANI-coated Si substrate and a bare Si substrate, using which InO$_x$ SIS was performed for different cycles (20, 50, 100, and 200 cycles). A major growth mechanism of the InO$_x$ samples is ALD-like because the PANI layer was absent on the Si substrate for the samples. The SIS samples were annealed at 280 °C for 1 h in a reducing atmosphere using a forming gas of 3% H$_2$ in N$_2$ gas. The thickness of the samples decreased by only ~2 nm after annealing owing to the densification of the composite film with a negligible decomposition of the PANI component. When the PANI−InO$_x$ samples were annealed in air, their thicknesses were significantly reduced, indicating the limited thermal stability of PANI in air. We used a four-point probe system to measure the electrical conductivity of the annealed samples.

Due to the impact of the film thickness on the surface scattering of charge carriers, the electrical conductivities of the InO$_x$ samples increased as the SIS cycle number increased (Figure 1b).[22] In contrast, PANI−InO$_x$ samples prepared with 50, 100, and 200 cycles exhibited conductivities of 4−9 S/cm without a clear trend with cycle numbers. This is because InO$_x$ was present mostly as a composite structure with PANI rather than as thin films on top of the PANI film. The electrical conductivities of the PANI−InO$_x$ samples after 20 cycles, as-grown PANI−InO$_x$ samples, and annealed PANI samples were below the measurable conductivity of the four-point probe equipment (~0.025 S/cm). The InO$_x$ network in the 20-cycle PANI−InO$_x$ samples may be less connected, leading to their nonmeasurable conductivities.[23] The poor conductivities of the as-grown samples were also understandable because the as-spun PANI was in the emeraldine base form of electrically insulating nature. InO$_x$ deposited by ALD or SIS at similar temperatures also displayed improved electrical conductivities after the annealing process.[23,24] Oxygen vacancies, which are induced by H$_2$−N$_2$ annealing, are well known to contribute to the electrical conductivities of InO$_x$ films by increasing electron concentrations.[25,26] In this work, the H$_2$−N$_2$ annealed PANI−InO$_x$ and InO$_x$ samples with 50 SIS cycles were selected as the main subjects of study to understand the compositional distribution, local chemical environments, and electrochemical properties of the "mixed" region of PANI and InO$_x$ components while possible contributions of pure InO$_x$ phases to them were minimized. The surface morphologies of the annealed PANI−InO$_x$ and InO$_x$ samples are similar, as shown in Figure 1c. These were also similar to the morphologies of the as-grown samples of each type, proving the thermal stability of the samples under the selected annealing conditions (Figure S2). The rough morphology is consistent with that of other InO$_x$ films grown at a growth temperature of 150 °C by thermal ALD.[27]

Figure 2a shows the distribution of the chemical composition of the PANI−InO$_x$ sample along the film direction. The depth profiles revealed that the InO$_x$ phase was present down to the bottom of the PANI film, although the In concentration gradually decreased along the film thickness. The distribution of the metal oxide in the polymer matrix in SIS is closely related to the infiltration kinetics of the precursors and the reactivity between the precursors and specific functional groups of the polymer.[16] As PANI does not contain precursor-reactive functional groups such as C=O, as in poly(methyl methacrylate), the spatial distribution of InO$_x$ in PANI is likely dominated by the temporal presence of TMIn molecules in the free volumes of PANI. The average mole fraction of In relative to O (i.e., [In]/([In] + [O])) in the
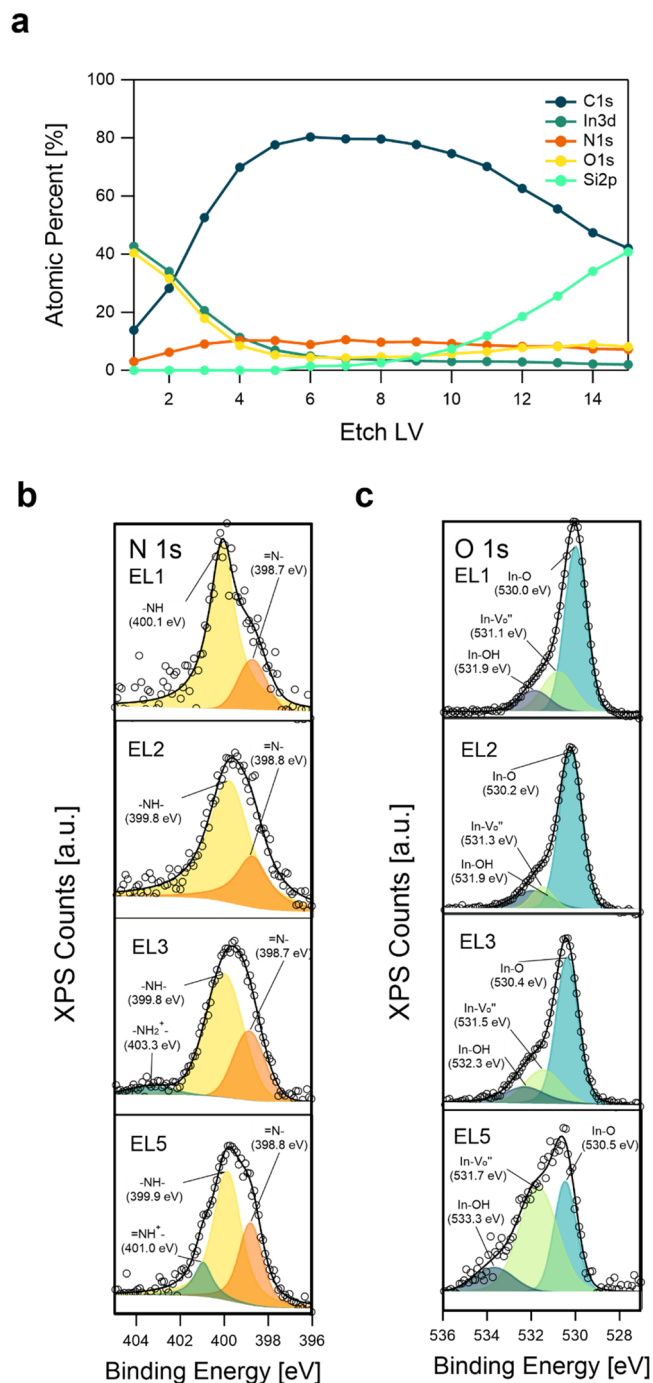
Figure 2. (a) XPS depth profile of the annealed PANI−InO$_x$ sample. The data is shown up to the 15th etch level (EL), which corresponds to the interface between the PANI−InO$_x$ film and the SiO$_2$ layer. (b) N 1s and (c) O 1s HRXPS of the same sample collected at different etch levels, as noted in the figure.

entire film region is ~41%, indicating the substoichiometric nature of the oxide (InO$_x$, $x \approx 1.44$).

Variations in the local chemical environments were investigated as a function of etch levels from N 1s (Figure 2b) and O 1s HRXPS (Figure 2c). The N 1s HRXPS spectra at different etch levels were deconvoluted into two to three peaks with the following assignments: (1) quinonoid imine (=N−) at ~398.5 eV, (2) benzenoid amine (−NH−) at ~399.5 eV; and (3) protonated amine and imine (−NH$_2^+$−, =NH$^+$−) at ~400 to ~402 eV.[28,29] Overall, the benzenoid amine

component was more dominant than the quinonoid imine component, suggesting a partial conversion of the quinonoid structure into the benzenoid structure. At certain etch levels, a small shoulder was observed at a higher BE, which was identified as a protonated imine or protonated amine group. The In−N bonding, which is expected to appear at a much lower BE (∼396.4 eV),[30] was absent in the HRXPS data collected at all etch levels, implying that the InO$_x$ and PANI phases were not completely homogenized but were present as two separate phases. Although the molecular structures of the PANI phase identified by HRXPS herein are consistent with those identified by other spectroscopic methods (vide infra), one needs to understand that the chemical states of different elements may be altered by Ar$^+$ ion sputtering during XPS depth profiling. Optimization of XPS conditions, such as ion beam energy and etch time, to minimize artifacts of ion beam damage may allow access to more accurate and quantitative information on the chemical states of PANI−InO$_x$. More recently, Ar cluster etching has been proven to cause no substantial damage to different polymers.[31] The most dominating component in O 1s HRXPS (Figure 2c) was an In−O peak at ∼530.5 eV, with shoulders at higher BEs assigned as In−V$_O^{••}$ (∼531.5 eV) and In−OH (∼532.5 eV) components. The presence of oxygen vacancies (V$_O^{••}$) is consistent with the substoichiometric nature of the oxide, as mentioned above. Similarly, composites of Ta$_2$O$_5$−SnO$_2$−PANI were reported to contain oxygen vacancies of high concentration along with N cation radicals, which are ascribed to the formation of the hybrid structures.[32] The proportion of the higher BE components is larger in the region closer to the Si substrate, which is consistent with the gradual blue shift of the In 3d peaks (Figure S4).

We then analyzed the effects of InO$_x$ SIS and H$_2$−N$_2$ annealing on the average molecular structures of the PANI phase via combined UV−vis spectroscopy, Raman spectroscopy, and FTIR spectroscopy. Figure 3a shows the UV−vis absorbance spectra of the as-spun PANI, as-grown PANI−InO$_x$, H$_2$−N$_2$ annealed PANI, and H$_2$−N$_2$ annealed PANI−InO$_x$. The pristine PANI film displayed two characteristic absorptions: (1) π−π * transition of the benzenoid ring at 320 nm and (2) n−π* transition between the benzenoid and quinonoid rings at 614 nm.[33,34] The spectral changes in the as-grown PANI−InO$_x$ and H$_2$−N$_2$ annealed PANI samples were similar in that the absorption by the benzenoid-to-quinonoid transition was suppressed. The annealed PANI−InO$_x$ sample displayed a further decrease in the transition at ∼614 nm. The absence of the 614 nm transition may indicate protonation of the quinonoid ring via either acid doping or oxidative doping.[19] However, in all of the samples, polaronic transition in the NIR range at wavelengths longer than ∼800 nm was also absent, implying a supportive role of the PANI phase in enhancing the electrical conductivities of the composite film. The band gap of InO$_x$ (∼3.6 eV) was less obvious in the H$_2$−N$_2$ annealed PANI−InO$_x$ after 50 cycles, but it was clearly seen in the sample after 200 SIS cycles (Figure S7).

The Raman spectra of the same set of samples are shown in Figure 3b. Table 1 summarizes the assignments of the Raman vibrational bands identified in the pristine PANI sample. The effects of InO$_x$ SIS and H$_2$−N$_2$ annealing were similar in that the intensities of the Raman bands were reduced because both processes perturbed the ordering of PANI chains. In the H$_2$−N$_2$ annealed PANI sample, the intensities of the bands at 1485 and 1164 cm^{-1} decreased more significantly compared to other
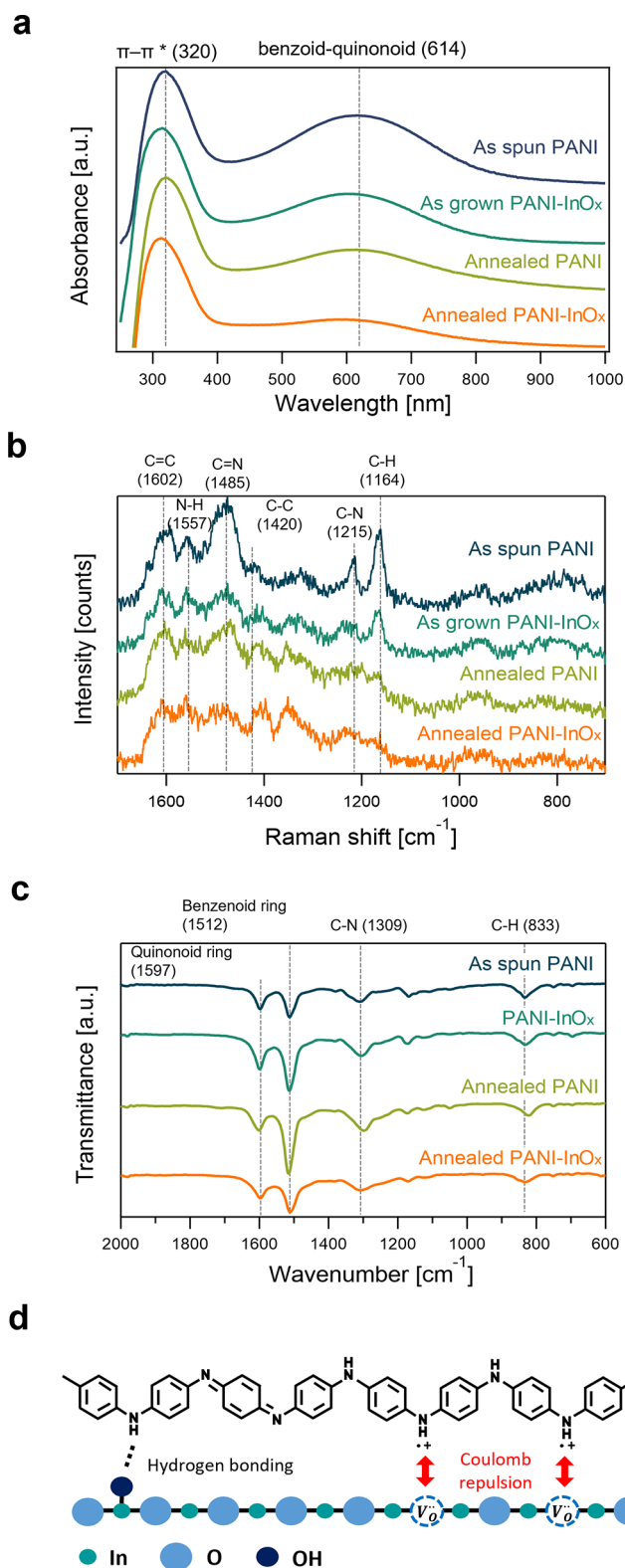
a

b

c

d

Figure 3. Comparisons of (a) UV−vis absorbance spectra, (b) Raman spectra, and (c) ATR-FTIR transmittance spectra for four different samples: as-spun PANI film, as-grown PANI−InO$_x$ film, annealed PANI, and annealed PANI−InO$_x$ film. The dashed lines in panel (b) mark the location of Raman bands observed in the as-spun PANI film, which were also summarized in Table 1. (d) Proposed structures of the interfaces between PANI and InO$_x$ phases.

Table 1. Major Raman Bands Identified in the Pristine PANI Sample[18,20,36]

wavenumber	assignment
1602	C=C stretching vibration of a quinonoid ring
1557	N−H bending
1485	C=N stretching vibrations in a quinonoid ring
1420	C−C stretching vibrations in a quinonoid ring
1215	C−N stretching in a benzenoid ring
1164	C−H deformation vibration of a quinonoid ring

bands, indicating the partial conversion of the quinonoid ring to the benzenoid ring, which is consistent with the UV−vis spectroscopy measurements. Interestingly, both annealed PANI and annealed PANI−InO$_x$ samples displayed a Raman band at ~1353 cm^{-1}, suggesting the presence of radical cations (C−N$^{\bullet+}$), consistent with the presence of protonated segments, as confirmed by the N 1s HRXPS.[20,35] The Raman band at 1420 cm^{-1} in the pristine PANI sample gradually shifted to a lower wavenumber with increased intensities after InO$_x$ SIS and annealing. A similar trend was observed in an earlier study on PANI doped with SnCl$_4$ and MoCl$_5$; however, the origin was unknown.[20]

We also analyzed ATR-FTIR transmittance spectra collected from the same set of samples (Figure 3c). All samples displayed four major IR modes: (1) stretching of the quinonoid ring at 1597 cm^{-1}, (2) stretching of the benzenoid ring at 1512 cm^{-1}, (3) C−N of secondary aromatic amine at 1309 cm^{-1}, and (4) out-of-plane C−H deformation of the 1,4-disubstituted aromatic ring at 833 cm^{-1}.[36] H$_2$−N$_2$ annealing resulted in a prominent enhancement of the stretching of the benzenoid ring relative to that of the quinonoid ring with red shifts of the C−N mode to 1298 cm^{-1} and the C−H mode to 821 cm^{-1}, all of which are clear indications of the transition from the benzenoid to the quinonoid ring structure. Similarly, the PANI−InO$_x$ and annealed PANI−InO$_x$ samples displayed a relative enhancement of the benzenoid ring stretching at ~1512 cm^{-1} compared to the quinonoid stretching at ~1599 cm^{-1}.

The combined characterization results of XPS, Raman spectra, and ATR-FTIR spectra showed the following: (1) the PANI phase has an enhanced benzenoid segment along with partial protonation, (2) the InO$_x$ phase contained not only lattice oxygen but also oxygen vacancies and −OH components, and (3) the In−N bonding was absent. Figure 3d shows the possible bonding and interaction at the interfaces between the PANI and InO$_x$ phases based on the above observations. First, hydrogen bonding between the H atoms in the benzenoid units and −OH in the InO$_x$ components may be present. Similarly, hydrogen bonding between the H atoms in the benzenoid units and the −OH components was observed in the PANI−CeO$_{2-\delta}$ composites.[37] Second, there could be Coulomb repulsion between the positively charged NH species in the protonated amine/imine segments and positively charged oxygen vacancies (V$_O^{\bullet\bullet}$). Similarly, stronger PANI−oxide interactions were observed in PANI−CeO$_{2-\delta}$ composites with a lower concentration of oxygen vacancies.[37] The presence of weak interactions (hydrogen bonding) and repulsion between the PANI and InO$_x$ phases, rather than the formation of strong bonds, can be related to the electrochemical properties of the composite samples, as described below.

Cyclic voltammograms (CVs) were collected from the three samples after H$_2$−N$_2$ annealing, PANI, PANI−InO$_x$, and InO$_x$ films, in an aqueous solution of pH 7 at a scan rate of 5 mV/s (Figure 4a). The thicknesses of the three samples were as
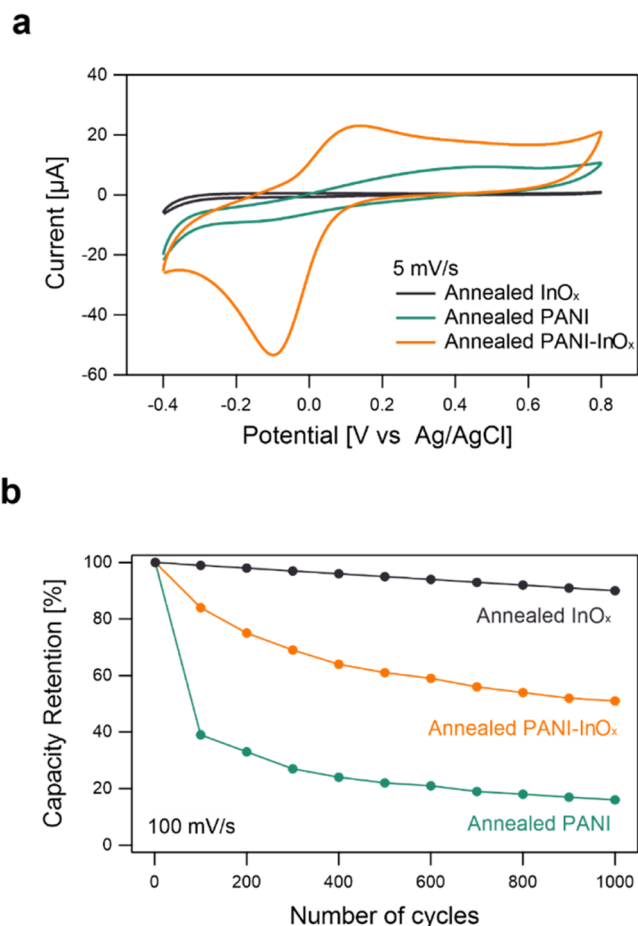

Figure 4. (a) CV curves of PANI−InO$_x$, PANI, and InO$_x$ samples collected at a scan rate of 5 mV/s in a pH 7 electrolyte. All samples were annealed before the CV measurements. (b) Retention of area-specific capacitance for the same set of samples used in panel (a).

follows: 32 nm for PANI, 45 nm for PANI−InO$_x$, and 15 nm for InO$_x$. The CV of the PANI−InO$_x$ sample displayed a well-defined pair of redox peaks with enhanced current densities compared to those of the InO$_x$ and PANI thin films. The origin of the redox peaks of the PANI−InO$_x$ sample is the conversion between the emeraldine and pernigraniline states, indicating the pseudocapacitive nature of the composite film. A gradual change in the potential of the redox peaks with respect to the electrolyte pH also implies that the redox reaction is accompanied by doping and de-doping of H$^+$ in PANI (Figure S8). For PANI in an acidic solution, there are commonly two pairs of redox peaks related to the conversion between the fully reduced leucoemeraldine state and the partially oxidized emeraldine state, and between the emeraldine state and the fully oxidized pernigraniline state. Protons are involved in the conversion reaction of emeraldine and pernigraniline. A gradual change in the potential of the redox peaks with respect to the change in pH of the electrolyte solution (Figure S8) implies that the origin of the redox peaks is from the conversion of the emeraldine and pernigraniline states, indicating the pseudocapacitive nature of the composite film.

The area-specific capacitance of the three samples was calculated using the following equation:

$$C_{sc} = \frac{\int I\,dV}{2v \cdot \Delta U \cdot A}$$

In this equation, $\int I\,dV$ is the integrated area of the CV, v is the scan rate, ΔU is the potential window, and A is the geometric area of the working electrode.[38] For this calculation, a nominal surface area of 1.2 cm^2 was assumed for all three samples. The calculated capacitance of PANI−InO$_x$ (1.96 mF/cm^2) was 3.5 times greater than that of PANI (0.55 mF/cm^2) and 28 times greater than that of InO$_x$ (0.07 mF/cm^2). Also, we carried out a two-electrode test using the same material as the positive and the negative electrodes. In the two-electrode test, the PANI−InO$_x$ samples displayed the highest capacitance among the three samples (Figure S9). The InO$_x$ SIS process induces surface roughening of the as-spun PANI film, which may contribute to an increase in the electrochemically active surface area of the composite film. The ECSA of the PANI−InO$_x$ sample was approximately 2.5 times greater than that of PANI, which was approximately 10 times greater than that of InO$_x$ (Figure S10). The trend in the calculated nominal capacitance among the three samples followed the same trend as the ECSA. Therefore, the enhanced capacitance of the PANI−InO$_x$ sample compared with that of the PANI sample may include the possible effects of surface roughening by SIS. Even with this caveat, the appearance of well-defined redox peaks in the PANI−InO$_x$ sample is a clear indication of improved electrochemical activity due to the synergistic effects between PANI and InO$_x$. Similar synergistic effects have been reported for capacitive applications in various kinds of composite materials such as composites of carbonaceous materials and metal oxides,[39,40] and those of metal−organic frameworks and conductive polymers,[41] which presented improved charge-transfer kinetics and improved electrical conductivity.

The PANI−InO$_x$ sample presented a nonlinear GCD curve with a potential plateau, indicating the battery-like nature of the sample (Figure S11). The GCD curve of the InO$_x$ sample had a triangular shape with similar charging and discharging times, consistent with the electrical double-layer capacitive (EDLC) nature, as observed in the CV of the sample (Figure 4). The PANI sample showed a slight deviation from the EDLC type, which could be due to the surface redox reaction corresponding to the different oxidation states of PANI. In the EIS test, all three samples displayed a small semicircle at higher frequencies and a straight line at lower frequencies (Figure S12). PANI−InO$_x$ displayed a semicircle with a smaller diameter among the samples, implying improved charge-transfer properties between the electrode surface and the electrolyte. The much lower capacitance of the as-grown PANI−InO$_x$ sample (Figure S13) also proves the critical role of electrically conductive InO$_x$. Interfaces of PANI−InO$_x$ containing oxygen vacancies may provide void sites in which ion diffusion and charge transfer are enhanced.[42,43] The highly enhanced electrochemical performance in a neutral condition is a distinctive feature in comparison to previous PANI-MO composites, which require acidic solutions for high electrochemical performances.[37,44−46] This result also implies that the fabricated PANI−InO$_x$ composites might also be used in application fields other than pseudocapacitors, such as electrochemical sensors with a wide pH range.[5] Recently, the partially protonated structure of PANI, which is similar to that of our PANI−InO$_x$ sample, was proposed as a promising cathode for aqueous zinc batteries by endowing more active sites.[47]

Figure 4b shows the retention test results of area-specific capacitance with respect to 1000 cycles for the same potential range at a scan rate of 100 mV/s. After the retention test, the PANI−InO$_x$ sample still displayed the largest capacitance (Figure S14) among the samples, although its retention property was between those of InO$_x$ and PANI. The gradual changes in the capacitance of the PANI−InO$_x$ sample may be related to further protonation in the PANI phase, as evidenced by the changes in the N 1s HRXPS and sample color after the retention test (Figure S15). Optimization of the InO$_x$ content in the PANI phase and the concentration of the oxygen vacancies may provide a viable way to improve the retention properties of composite structures.[37] Future studies of interest will be the application of SIS into CP in different forms for a higher surface area because the structures with high surface areas will further amplify the synergistic effects of the PANI−InO$_x$ composites.

■ CONCLUSIONS

In summary, we have reported the SIS of PANI−InO$_x$ hybrid thin films and explored their potential for use in electrochemical energy storage. The annealed PANI−InO$_x$ hybrid thin films with 50−200 SIS cycles exhibited electrical conductivities of 4−9 S/cm. The hybrid thin films displayed a graded concentration of InO$_x$ along the direction of the film thickness, with a higher concentration of oxygen vacancies in the PANI-rich region. The combined characterization of the composite films via UV−vis spectroscopy, Raman spectroscopy, and FTIR spectroscopy revealed that the quinonoid structure in PANI was partially converted to a benzenoid structure along with partial protonation. The composite film displayed higher pseudocapacitive capabilities with a pair of distinctive redox peaks compared to single-phase InO$_x$ films and single-phase PANI films, which are probably related to the interfaces of PANI−InO$_x$ containing oxygen vacancies and protonated amine/imine units that can enable enhanced ion diffusion and charge transfer.

■ ASSOCIATED CONTENT

ⓈI Supporting Information

The Supporting Information is available free of charge at https://pubs.acs.org/doi/10.1021/acsomega.2c06309.

> Vapor pressure test of trimethylindium; SEM images of as-grown PANI-InOx and as-grown InO$_x$; thermogravimetric analysis; In 3d HRXPS of annealed PANI−InO$_x$; Tauc plot of the annealed PANI−InO$_x$; CV of the annealed PANI−InO$_x$ at various solution pH values; ECSA of annealed PANI−InO$_x$, PANI and InO$_x$; CV of the as-grown PANI−InO$_x$; GCD and EIS tests of annealed PANI−InO$_x$, InO$_x$, and PANI; CV retention test curves of the annealed PANI−InO$_x$, InO$_x$, and PANI; pictures of the annealed PANI−InO$_x$ and PANI after CV retention test; and N 1s HRXPS of the annealed PANI−InO$_x$ (PDF)

■ AUTHOR INFORMATION

Corresponding Author

Nari Jeon − *Department of Materials Science and Engineering, Chungnam National University, Daejeon 34134, Republic of Korea;* ● orcid.org/0000-0002-8240-744X; Email: njeon@cnu.ac.kr

Authors

Jiwoong Ham − *Department of Materials Science and Engineering, Chungnam National University, Daejeon 34134, Republic of Korea;* ● orcid.org/0000-0001-7602-7566

Sangbaek Park − *Department of Materials Science and Engineering, Chungnam National University, Daejeon 34134, Republic of Korea;* ● orcid.org/0000-0002-4900-2010

Complete contact information is available at:
https://pubs.acs.org/10.1021/acsomega.2c06309

Notes

The authors declare no competing financial interest.

■ REFERENCES

(1) Zare, E. N.; Motahari, A.; Sillanpää, M. Nanoadsorbents based on conducting polymer nanocomposites with main focus on polyaniline and its derivatives for removal of heavy metal ions/dyes: A review. *Environ. Res.* 2018, 162, 173−195.

(2) Uppalapati, D.; Boyd, B. J.; Garg, S.; Travas-Sejdic, J.; Svirskis, D. Conducting polymers with defined micro- or nanostructures for drug delivery. *Biomaterials* 2016, 111, 149−162.

(3) Zhou, Q.; Shi, G. Conducting Polymer-Based Catalysts. *J. Am. Chem. Soc.* 2016, 138, 2868−2876.

(4) Fu, L.; Qu, Q.; Holze, R.; Kondratiev, V. V.; Wu, Y. Composites of metal oxides and intrinsically conducting polymers as super-capacitor electrode materials: the best of both worlds? *J. Mater. Chem.* 2019, 7, 14937−14970.

(5) Peng, S.; Yu, Y.; Wu, S.; Wang, C.-H. Conductive Polymer Nanocomposites for Stretchable Electronics: Material Selection, Design, and Applications. *ACS Appl. Mater. Interfaces* 2021, 13, 43831−43854.

(6) Choi, S.; Han, S. I.; Kim, D.; Hyeon, T.; Kim, D.-H. High-performance stretchable conductive nanocomposites: materials, processes, and device applications. *Chem. Soc. Rev.* 2019, 48, 1566−1595.

(7) Thomas, S. W.; Khan, R. R.; Puttananjegowda, K.; Serrano-Garcia, W.Chapter 9 - Conductive polymers and metal oxide polymeric composites for nanostructures and nanodevices. In *Advances in Nanostructured Materials and Nanopatterning Technologies*; Guarino, V.; Focarete, M. L.; Pisignano, D., Eds.; Elsevier, 2020; pp 243−271.

(8) Ren, Y.; Qing, L.; Li, L.; Hasichaolu; Zheng, H.; Ou, K. Facile synthesis of highly conductive polymer fiber for application in flexible fringing field capacitive sensor. *Sens. Actuator A Phys.* 2022, 342, No. 113616.

(9) Xue, J.; Mo, M.; Liu, Z.; Ye, D.; Cheng, Z.; Xu, T.; Qu, L. A general synthesis strategy for the multifunctional 3D polypyrrole foam of thin 2D nanosheets. *Front. Mater. Sci.* 2018, 12, 105−117.

(10) Zhao, F.; Shi, Y.; Pan, L.; Yu, G. Multifunctional Nano-structured Conductive Polymer Gels: Synthesis, Properties, and Applications. *Acc. Chem. Res.* 2017, 50, 1734−1743.

(11) Cara, E.; Murataj, I.; Milano, G.; De Leo, N.; Boarino, L.; Ferrarese Lupi, F. Recent Advances in Sequential Infiltration Synthesis (SIS) of Block Copolymers (BCPs). *Nanomaterials* 2021, 11, No. 994.

(12) Waldman, R. Z.; Mandia, D. J.; Yanguas-Gil, A.; Martinson, A. B. F.; Elam, J. W.; Darling, S. B. The chemical physics of sequential infiltration synthesis-A thermodynamic and kinetic perspective. *J. Chem. Phys.* 2019, 151, No. 190901.

(13) Shi, L.-Y.; Subramanian, A.; Weng, L.; Lee, S.; Kisslinger, K.; Nam, C.-Y.; Ross, C. A. Selective sequential infiltration synthesis of ZnO in the liquid crystalline phase of silicon-containing rod-coil block copolymers. *Nanoscale* 2022, 14, 1807−1813.

(14) Pleshek, D.; Tran, J.; Li, Y.; Shirani, A.; Shevchenko, E. V.; Berman, D. Swelling-Assisted Sequential Infiltration Synthesis of Nanoporous ZnO Films with Highly Accessible Pores and Their Sensing Potential for Ethanol. *ACS Appl. Mater. Interfaces* 2021, 13, 35941−35948.

(15) Ren, Y.; McGuinness, E. K.; Huang, C.; Joseph, V. R.; Lively, R. P.; Losego, M. D. Reaction−Diffusion Transport Model to Predict Precursor Uptake and Spatial Distribution in Vapor-Phase Infiltration Processes. *Chem. Mater.* 2021, 33, 5210−5222.

(16) Ham, J.; Ko, M.; Choi, B.; Kim, H.-U.; Jeon, N. Understanding Physicochemical Mechanisms of Sequential Infiltration Synthesis toward Rational Process Design for Uniform Incorporation of Metal Oxides. *Sensors* 2022, 22, No. 6132.

(17) Weisbord, I.; Shomrat, N.; Azoulay, R.; Kaushansky, A.; Segal-Peretz, T. Understanding and Controlling Polymer−Organometallic Precursor Interactions in Sequential Infiltration Synthesis. *Chem. Mater.* 2020, 32, 4499−4508.

(18) Wang, W.; Chen, C.; Tollan, C.; Yang, F.; Beltrán, M.; Qin, Y.; Knez, M. Conductive Polymer−Inorganic Hybrid Materials through Synergistic Mutual Doping of the Constituents. *ACS Appl. Mater. Interfaces* 2017, 9, 27964−27971.

(19) Gregory, S. A.; Li, Y.; Monroe, T. D.; Li, J.; Yee, S. K.; Losego, M. D. Vapor Phase Infiltration Doping of the Semiconducting Polymer Poly(aniline) with $TiCl_4 + H_2O$: Mechanisms, Reaction Kinetics, and Electrical and Optical Properties. *ACS Appl. Polym. Mater.* 2021, 3, 720−729.

(20) Wang, W.; Yang, F.; Chen, C.; Zhang, L.; Qin, Y.; Knez, M. Tuning the Conductivity of Polyaniline through Doping by Means of Single Precursor Vapor Phase Infiltration. *Adv. Mater. Interfaces* 2017, 4, No. 1600806.

(21) Wang, C.; Yu, H.-Y.; Miao, Z.; Ge, D.; Abdalkarim, S. Y. H.; Yao, J. Interface Growth of PANI-ZnO Nanohybrids on a Self-Formed Grapefruit Peel Aerogel to Construct a Quick Self-Restored Gas Sensor. *ACS Sustainable Chem. Eng.* 2022, 10, 6573−6583.

(22) Lee, S.; Kim, M.; Cho, S.-Y.; Lee, D.-J.; Kim, H.-M.; Kim, K.-B. Electrical properties of graphene/In2O3 bilayer with remarkable uniformity as transparent conducting electrode. *Nanotechnology* 2019, 31, No. 095708.

(23) Taggart, A. D.; Jeon, N.; Rozyyev, V.; Karapetrova, E.; Zaluzec, N. J.; Waldman, R. Z.; Darling, S. B.; Elam, J. W.; Martinson, A. B. F. Electronic Conductivity of Nanoporous Indium Oxide Derived from Sequential Infiltration Synthesis. *J. Phys. Chem. C* 2021, 125, 21191−21198.

(24) Mane, A. U.; Allen, A. J.; Kanjolia, R. K.; Elam, J. W. Indium Oxide Thin Films by Atomic Layer Deposition Using Trimethylin-dium and Ozone. *J. Phys. Chem. C* 2016, 120, 9874−9883.

(25) Bierwagen, O. Indium oxide-a transparent, wide-band gap semiconductor for (opto)electronic applications. *Semicond. Sci. Technol.* 2015, 30, No. 024001.

(26) Galazka, Z.; Irmscher, K.; Pietsch, M.; Schulz, T.; Uecker, R.; Klimm, D.; Fornari, R. Effect of heat treatment on properties of melt-

grown bulk In2O3 single crystals. *CrystEngComm* **2013**, *15*, 2220−2226.

(27) Agbenyeke, R. E.; Jung, E. A.; Park, B. K.; Chung, T.-M.; Kim, C. G.; Han, J. H. Thermal atomic layer deposition of In2O3 thin films using dimethyl(N-ethoxy-2,2-dimethylcarboxylicpropanamide)indium and H2O. *Appl. Surf. Sci.* **2017**, *419*, 758−763.

(28) Liu, F.; Luo, S.; Liu, D.; Chen, W.; Huang, Y.; Dong, L.; Wang, L. Facile Processing of Free-Standing Polyaniline/SWCNT Film as an Integrated Electrode for Flexible Supercapacitor Application. *ACS Appl. Mater. Interfaces* **2017**, *9*, 33791−33801.

(29) Li, P.; Jin, Z.; Peng, L.; Zhao, F.; Xiao, D.; Jin, Y.; Yu, G. Stretchable All-Gel-State Fiber-Shaped Supercapacitors Enabled by Macromolecularly Interconnected 3D Graphene/Nanostructured Conductive Polymer Hydrogels. *Adv. Mater. Lett.* **2018**, *30*, No. 1800124.

(30) Deminskyi, P.; Rouf, P.; Ivanov, I. G.; Pedersen, H. Atomic layer deposition of InN using trimethylindium and ammonia plasma. *J. Vac. Sci. Technol., A* **2019**, *37*, No. 020926.

(31) Hofstetter, Y. J.; Vaynzof, Y. Quantifying the Damage Induced by X-ray Photoelectron Spectroscopy Depth Profiling of Organic Conjugated Polymers. *ACS Appl. Polym. Mater.* **2019**, *1*, 1372−1381.

(32) Aranthady, C.; Shanbhag, G. V.; Sundaram, N. G. Polyaniline/(Ta2O5−SnO2) hybrid nanocomposite for efficient room temperature CO gas sensing. *RSC Adv.* **2022**, *12*, 15759−15766.

(33) Li, Z.; Li, Y.; Lin, W.; Zheng, F.; Laven, J. Polyaniline/silver nanocomposites synthesized via UV−Vis-assisted aniline polymerization with a reversed micellar microemulsion system. *Polym. Compos.* **2016**, *37*, 1064−1071.

(34) Xu, P.; Han, X.; Wang, C.; Zhang, B.; Wang, X.; Wang, H.-L. Facile Synthesis of Polyaniline-Polypyrrole Nanofibers for Application in Chemical Deposition of Metal Nanoparticles. *Macromol. Rapid Commun.* **2008**, *29*, 1392−1397.

(35) Fujisaki, T.; Kashima, K.; Serrano-Luginbühl, S.; Kissner, R.; Bajuk-Bogdanović, D.; Milojević-Rakić, M.; Ćirić-Marjanović, G.; Busato, S.; Lizundia, E.; Walde, P. Effect of template type on the preparation of the emeraldine salt form of polyaniline (PANI-ES) with horseradish peroxidase isoenzyme C (HRPC) and hydrogen peroxide. *RSC Adv.* **2019**, *9*, 33080−33095.

(36) Trchová, M.; Morávková, Z.; Bláha, M.; Stejskal, J. Raman spectroscopy of polyaniline and oligoaniline thin films. *Electrochim. Acta* **2014**, *122*, 28−38.

(37) Kuzmanović, B.; Vujković, M. J.; Tomić, N.; Bajuk-Bogdanović, D.; Lazović, V.; Šljukić, B.; Ivanović, N.; Mentus, S. The influence of oxygen vacancy concentration in nanodispersed non-stoichiometric CeO2-δ oxides on the physico-chemical properties of conducting polyaniline/CeO2 composites. *Electrochim. Acta* **2019**, *306*, 506−515.

(38) Liu, T.; Finn, L.; Yu, M.; Wang, H.; Zhai, T.; Lu, X.; Tong, Y.; Li, Y. Polyaniline and Polypyrrole Pseudocapacitor Electrodes with Excellent Cycling Stability. *Nano Lett.* **2014**, *14*, 2522−2527.

(39) Chen, L.; Xu, X.; Wan, L.; Zhu, G.; Li, Y.; Lu, T.; Albaqami, M. D.; Pan, L.; Yamauchi, Y. Carbon-incorporated Fe3O4 nanoflakes: high-performance faradaic materials for hybrid capacitive deionization and supercapacitors. *Mater. Chem. Front.* **2021**, *5*, 3480−3488.

(40) Li, Y.; Zhu, G.; Xu, X.; Chen, L.; Lu, T.; Hill, J. P.; Pan, L.; Yamauchi, Y. Embedding Metal−Organic Frameworks for the Design of Flexible Hybrid Supercapacitors by Electrospinning: Synthesis of Highly Graphitized Carbon Nanofibers Containing Metal Oxide Nanoparticles. *Small Struct.* **2022**, *3*, No. 2200015.

(41) Xu, X.; Tang, J.; Qian, H.; Hou, S.; Bando, Y.; Hossain, M. S. A.; Pan, L.; Yamauchi, Y. Three-Dimensional Networked Metal−Organic Frameworks with Conductive Polypyrrole Tubes for Flexible Supercapacitors. *ACS Appl. Mater. Interfaces* **2017**, *9*, 38737−38744.

(42) Bi, W.; Jahrman, E.; Seidler, G.; Wang, J.; Gao, G.; Wu, G.; Atif, M.; AlSalhi, M.; Cao, G. Tailoring Energy and Power Density through Controlling the Concentration of Oxygen Vacancies in V2O5/PEDOT Nanocable-Based Supercapacitors. *ACS Appl. Mater. Interfaces* **2019**, *11*, 16647−16655.

(43) Bi, W.; Wu, Y.; Liu, C.; Wang, J.; Du, Y.; Gao, G.; Wu, G.; Cao, G. Gradient Oxygen Vacancies in V2O5/PEDOT Nanocables for High-Performance Supercapacitors. *ACS Appl. Energy Mater.* **2019**, *2*, 668−677.

(44) Huang, J.; Wang, Z.; Hou, M.; Dong, X.; Liu, Y.; Wang, Y.; Xia, Y. Polyaniline-intercalated manganese dioxide nanolayers as a high-performance cathode material for an aqueous zinc-ion battery. *Nat. Commun.* **2018**, *9*, No. 2906.

(45) Wei, H.; Yan, X.; Wu, S.; Luo, Z.; Wei, S.; Guo, Z. Electropolymerized Polyaniline Stabilized Tungsten Oxide Nanocomposite Films: Electrochromic Behavior and Electrochemical Energy Storage. *J. Phys. Chem. C* **2012**, *116*, 25052−25064.

(46) Gautam, K. P.; Acharya, D.; Bhatta, I.; Subedi, V.; Das, M.; Neupane, S.; Kunwar, J.; Chhetri, K.; Yadav, A. P. Nickel Oxide-Incorporated Polyaniline Nanocomposites as an Efficient Electrode Material for Supercapacitor Application. *Inorganics* **2022**, *10*, No. 86.

(47) Yan, H.; Mu, X.; Song, Y.; Qin, Z.; Guo, D.; Sun, X.; Liu, X.-X. Protonating imine sites of polyaniline for aqueous zinc batteries. *Chem. Commun.* **2022**, *58*, 1693−1696.